

GHz-rate optical phase shift in light matter
interaction-engineered, silicon-ferroelectric nematic liquid
crystals

Iman Taghavi^{1,2*}, Omid Esmaeeli¹, Sheri Jahan Chowdhury¹, Matthew Mitchell²,
Donald Witt^{1,3}, Cory Pecinovsky⁴, Jason Sickler⁴, Nicolas A.F. Jaeger¹,
Sudip Shekhar^{1,2,5*}, and Lukas Chrostowski^{1,2,3*}

¹Department of Electrical and Computer Engineering, University of British Columbia, 2332
Main Mall, Vancouver, V6T 1Z4, B.C., Canada.

²Dream Photonics, 2366 Main Mall, Vancouver, B.C., Canada.

³Quantum Matter Institute, University of British Columbia, 2355 E Mall, Vancouver, V6T
1Z4, B.C., Canada.

⁴Polaris Electro-Optics, 3400 Industrial Ln, 3130 25th St, Broomfield, 80020, CO, USA.

⁵Dream Photonics Inc., Woodinville, WA, USA.

*Corresponding author(s). E-mail(s): staghavi3@ece.ubc.ca; sudip@ece.ubc.ca;
lukasc@ece.ubc.ca;

Abstract

Organic electro-optic (OEO) materials have demonstrated promising performance in developing electro-optic phase shifters (EOPS) and modulators compared to their inorganic counterparts. Integration with other devices in a silicon photonic (SiP) process, simple nanofabrication, and temperature/aging robustness remain to be developed for this class of hybrid material platforms. In particular, electro-optic (EO) polymers need an electro-thermal poling method, which has limited their potential

and utilization in large-scale SiP. Devices made of paraelectric nematic liquid crystals (PN-LC), another primary type of OEO material, feature a very efficient but slow phase shift mechanism.

We present a general-purpose EOPS that applies to various modulator embodiments to address these concerns. Based on that, we report a GHz-fast phase shift in a newly discovered family of OEO, namely ferroelectric nematic liquid crystals (FN-LC), which finally enables liquid crystals to have significant second-order nonlinear optical coefficients and associated Pockels effect. The new material avoids poling issues associated with EO polymers and can pave the way for hybrid silicon-OEO systems with CMOS-foundry compatibility. Furthermore, we propose a finger-loaded, non-slotted waveguide that enhances light-matter interaction, allowing us to achieve DC and AC modulation efficiencies of $\approx 0.25 \text{ V}\cdot\text{mm}$ and $25.7 \text{ V}\cdot\text{mm}$, respectively, an on-chip insertion loss of $\approx 4 \text{ dB}$, and an EO bandwidth of $f_{-6\text{dB}} > 4.18 \text{ GHz}$. The remaining figures of merit for our poling-free EOPS are equivalent to EO polymer-enabled devices with fewer manufacturing difficulties. We demonstrate an electrically and photonicallly packaged chip that contains >100 silicon-FN-LC modulators to evaluate the large-scale integration of our poling-free phase shifters and modulators.

Keywords: Silicon organic hybrid material, electro optic polymer, liquid crystal, phase shifter, modulator

Silicon and silicon nitride photonics have enabled several recent technological advancements, and future roadmaps have been designed based on their capabilities and integration with established CMOS foundries [1]. The electro-optic phase shifter (EOPS) [2–5] is one of the most fundamental components upon which other essential building blocks in photonic integrated circuits (PIC) are based, including electro-optic (EO) switches [6–8], EO modulators [9], optical interconnects [10–12], and comb generators [13]. Traditional phase shift mechanisms often show poor overall performance, such as limited EO bandwidth (BW) and high static energy consumption (E_{stat}) when leveraging the thermo-optic effect or free-carrier dispersion effect with traveling wave modulators. Free carrier dispersion also leads to doping-induced insertion loss (IL). Innovations in hybrid material platforms promise novel solutions to traditional Si

photonics (SiP) shortcomings. However, they typically face significant challenges, such as several complex nanofabrication stages, scaling, and interaction with current CMOS foundries. Modulators based on indium tin oxide (ITO) have recently experienced notable improvements [9, 14–16]. The additional operations necessary for ITO/insulator thin-film deposition, demanding quality control methods, and their low extinction ratio (ER) suggest further R&D needs [17]. Carrier-free phase shift processes, such as the Pockels effect, are among the more appealing techniques, especially regarding EO BW and energy consumption. These metrics and low IL can excel in LiNbO₃ on silicon (LNOI) [18]. Due to the low EO coefficient of LiNbO₃, however, phase shifters based on LNOI require either a large footprint or a high drive voltage (V_π), where V_π is the voltage necessary to produce the π shift. A material system based on barium titanate (BTO) can simultaneously meet the requirements of low IL and high EO BW [19, 20]. Despite having a significant EO coefficient, BTO is unable to fully utilize the improved light-matter interactions (LMI) provided by some waveguide topologies, such as slot waveguides, failing to give the record-low modulation efficiencies ($V_\pi L$), where L is the EOPS effective length [21]. BTO also involves more meticulous fabrication steps, loses its high EO efficiency at cryogenic temperatures, and necessitates process controls for optimum domain development [22].

Furthermore, the preceding approaches cannot meet the trade-offs between various device metrics of a particular modulator, such as size, EO and optical BW, IL, V_π , E_{stat} , and dynamic energy consumption (E_{dyn}) [23, 24]. Hybrid integration of Si with organic electro-optic (OEO) materials has been proposed to overcome this shortcoming. They have advantages over their inorganic equivalents due to a combination of their EO and physicochemical characteristics. The EO properties of OEO materials, including the Pockels factor ($n^3 r_{33}$) and optical loss, have continuously progressed over the last two decades ($n^3 r_{33}$ as large as 9000 pm/V and absorption coefficients as low as 1.8×10^{-5} have been reported [25], where n is the OEO refractive index and r_{33} represents the Pockels coefficient). Thanks to their liquid state, an OEO can infiltrate nanostructures during the coating step and benefit from the enhanced LMI. Along with the resultant high modulation efficiencies, the low dielectric dispersion [26] of OEO promises better modulators. As a result, <1 V, sub-mm-long Mach-Zehnder modulators (MZM) with IL < 1 dB, EO BW surpassing 100 GHz, and $E_{\text{dyn}} < 100$ fJ/bit have been enabled [27]. Such an all-inclusive, miniaturized modulator can work in extreme temperatures (as high as 383 K (110°C) [28] and as low as 4 K [29, 30]), which encompass the crucial requirements for a state-of-the-art modulator.

While EO polymers have attracted increased attention mainly because of their remarkable EO characteristics, their application to photonic-integrated circuits (PIC) has challenges. Multiple process steps and often hazardous solvents are needed to prepare EO polymer thin films, necessitating equipment for precise mixing, coating, and drying. In addition, to align chromophores in an EO polymer material, an electro-thermal poling step is necessary. Depending on the waveguide geometry and accompanying LMI, dedicated DC lines may be required on a larger scale. Despite considerable breakthroughs in producing thermally and temporally stable polymers, not all poled polymers are resilient to high temperatures ([28]), aging ([31]), and poling-induced optical loss ([32]). For practical applications, the devices may still require a certain level of hermetic sealing to become temperature- and humidity-resistant. EO polymers are also recognized for their lower resistance at higher temperatures, which coincides with detrimental leakage currents. It leads to decreased EO efficiency, which has a direct impact on device performance. Additional nanofabrication steps have been identified as advantageous to resolving this issue, such as exploiting a thin charge-barrier layer comprised of alumina or titania created by atomic layer deposition,[33, 34]. Poling also limits high-temperature excursions typical of back end-of-line (BEOL) processing since such excursions would destroy the poling-induced order. The problems above could increase the overall cost, add complexity, and jeopardize the integration of polymer-based hybrid platforms.

Another class of OEO material is PN-LC, which provides a variety of efficient but slow phase shift processes, such as the birefringence effect [3, 35–37]. Ultra-high modulation efficiencies have been reported using strong-LMI implementations, including infiltrated slot waveguides with the material [2]. Unlike polymers, preparing PN-LC devices do not involve a solvent that must be evaporated during post-baking processes. It simplifies the spin coating process and may allow for new coating approaches. The material, for example, can be coated on photonic parts via microfluidic channels or fluid dispensing. A PN-LC-based platform is attractive for realizing EO switches, phase shifters, or shutters, but it is not desirable for high-speed applications.

A new state of matter, ferroelectric nematic liquid crystals (FN-LC), has recently been discovered [38, 39]. In the landscape of organic EO materials, FN-LCs are situated between poled polymers, organic nonlinear optic (NLO) crystals, and PN-LCs, bringing the most desirable aspects of each (see table I). Like poled polymers and organic NLO crystals, FN-LCs are non-centrosymmetric and have nonzero second-order susceptibilities ($\chi^{(2)}$). Like organic NLO

crystals and PN-LCs, they organize spontaneously—the ordered state is the thermodynamic minimum with significant order parameters. Similar to PN-LCs, the alignment can be controlled over large areas by applying alignment layers at the interface or small external fields. They can also be switched like PN-LCs, with a reorientation of the fast and slow axes in an external field. A unique feature of the FN-LC is that the molecular long axis (slow axis) is highly polarizable and coincident with the director and the polar axis (Fig. 1(a) inset). This creates the condition for achieving very large spontaneous polarizations and large second order nonlinearities, which have been observed by second harmonic generation measurements [40]. These nonlinearities have been dramatically enhanced by adding NLO dyes to the polar matrix of the FN-LC host material [41]. However, what remains to be demonstrated is the EO effect (i.e., Pockels effect) observed in other non-centrosymmetric organic materials. In this work, we show that FN-LCs can be integrated with similar ease as PN-LCs onto a SiP platform, that alignment of the polar axis can be easily achieved over the length of the device, and that a significant EO response can be observed.

To enhance LMI, waveguides such as Si [42] and plasmonic [43] slotted, sub-wavelength grating (SWG) [44], photonic-crystal [45], and thinned [28], would traditionally be used as EOPS in modulators. However, they often add excessive loss [46], limit optical BW, and need extra fabrication stages, some of which are not quite CMOS-compatible. For instance, opening oxide cladding over isolated Si islands of SWG or metallic slots of plasmonic waveguides may violate design rules in wafer nanofabrication. Also, exploiting the benefits of structures such as thinned waveguides necessitates escalators from complete to partial etch Si, which are not readily available. Geometries required for efficient and low-loss mode converters, such as strip-to-slot, are not always accessible through nanofabrication runs or have integration challenges with the rest of the PIC. On the other hand, a non-slotted waveguide does not have these issues at the cost of offering a weak LMI [47], thus requiring a high voltage for poling and driving. The device size and EO BW must then be compromised to keep the voltage within the ranges supplied by CMOS drivers.

We propose a finger-loaded non-slotted (FNS) waveguide consisting of two strip-to-finger-loaded mode converters to resolve this trade-off, as seen in Fig. 1(a). In analogy to segmented slotted [48] and non-slotted [49] topologies, this structure eliminates the misalignment problem seen in strip-loaded slot waveguides by offering at least one fewer step for the nanofabrication of the partially etched slab layers. The periodicity and duty cycle of the subwavelength structure

of the FNS waveguide are selected to produce a better balance between electrical and optical loss penalties, another prevalent difficulty in slot waveguides. The waveguide core, sandwiched between fingers, is narrowed to $W_c = 300$ nm to localize light in the gap between them, as seen in Fig. 2. Compared to a nonslotted structure, the overlap integral between optical (\hat{E}_x) and electrical (\vec{E}_e) modal fields (Γ) is enhanced by a factor of ≈ 2 . At the same time, the effective electrode separation is ≈ 10 times smaller. Consequently, the essential figure of merit evaluated by the modulation efficiency-loss product (i.e., $V_\pi L \alpha$) remains ≈ 5 times better despite the excess loss caused by the subwavelength structure of the FNS topology. Our simulations revealed that strip-to-finger-loaded mode converters did not substantially impact total EOPS loss. Due to its SWG structure, FNS topology utilizes capillary force action to mitigate material infiltration, another ubiquitous issue in slot waveguides that frequently calls for oxide undercutting [50].

The constructed devices must then be aligned with an electric field. Because of its pre-ordered molecular orientation and sensitivity to an external field, FN-LC was found to be fully aligned with ≈ 10 times smaller \vec{E}_e than required for poling EO polymers [51], for similar waveguide structures. The process was carried out at room temperature; no precise temperature monitor was necessary. These relaxed voltage and temperature conditions have additional advantages. First, an inert gas such as N_2 is not required around the chip during alignment to avoid oxidation. The FN-LC alignment process is relatively safer because there is no off-gassing. Within the scope of our characterization setup, the device's performance exhibited little temperature susceptibility thanks to the non-electro-thermal alignment technique. To be more precise, no performance aging was discovered for the FN-LC-coated devices over 150 hours of operation in the range of $10 \sim 50^\circ\text{C}$ under full optical and electrical load. EO polymers lose their poling efficiency beyond their glass transition temperature ($\approx 80 \sim 100^\circ\text{C}$). To show that FN-LC is useful at these temperatures, more accelerated aging tests must be done in the future. The lower voltage required for alignment simplifies design concerns for the large-scale integration of FN-LC-enabled photonic devices in which the same RF lines can be utilized. Finally, a fully-aligned FN-LC MZM showed ≈ 2 to 3 dB less material absorption loss, which we attribute to the formation of a monodomain over the length of the device and reduced scattering loss.

Monitoring optical loss and leakage current throughout the alignment process provides critical information. As seen in Fig. 3(a)-(b), changes in optical loss followed by saturation indicate

that domain formation has been completed. In some cases, the change was permanent, indicating that the optic axis continues to remain in a vertical posture. Following the alignment, we performed DC characterization of the optical transmission, as shown in Fig. 3(c), achieving an optical ER of ≈ 26 dB and $V_{\pi,DC} \approx 0.5$ V. The birefringence effect is responsible for this considerable shift.

A more comprehensive figure of merit for a given EOPS is the pure phase efficiency (η_{pps}). The metric is defined as $(\partial n/\partial v) / (\partial \kappa/\partial v)$, where n and κ are the real and imaginary parts of the complex refractive index ($n + i\kappa$), respectively. V_{π} and loss can be correlated to the estimated values for $\partial n/\partial v$ and $\partial \kappa/\partial v$. The optical ER, $V_{\pi}L\alpha$, η_{pps} comprise a comprehensive assessment of EOPS appropriateness as summarized in Table 2. For our proposed FNS waveguide, significantly higher records up to $\eta_{\text{pps}} \approx 88.9$ have been achieved. We believe the proposed EOPS' improved phase shift performance stems from combining our device design and the material.

Without a high-speed phase shift mechanism, FN-LC might not demonstrate any significant benefit over traditional PN-LC, in which the slower mechanisms mostly dominate the response. Various aspects of such a frequency response characterization of the FN-LC-coated devices are shown in Fig. 4, and the measurement details are covered in Methods. SWG-based grating couplers (GC) were used for light injection into the devices for this step [52–54]. The S -parameter collected by a Vector Network Analyzer (VNA) indicates that $f_{-6\text{dB}} > 4.18$ GHz. This achievement demonstrates a phase shift mechanism with a rise/fall time in the nanosecond range, while PN-LC is limited to functioning in the millisecond range [2]. Accordingly, we employed S_{21} data and an analytical approach (see Methods) to evaluate the EO properties of the FN-LC material and the proposed EOPS. As a result, an EO coefficient of $r_{33} \approx 24$ pm/V and an AC modulation efficiency of $V_{\pi}L \approx 25.7$ (V·mm) were estimated. The metrics are still significantly lower than the maximum record for EO polymers. This being the first demonstration, promises further improvement in the future. The frequency span of the response was confined to the equipment and electrical wire bonding (EWB) used to drive the EOPS. Nonetheless, it appears that the FN-LC phase shift mechanism switches from a strong birefringence effect at low frequencies to a weaker but faster Pockels effect at higher frequencies. Complex phase manipulation is frequently necessary to implement advanced modulation systems, such as coherent transceivers [55]. Inefficient thermal heaters are commonly employed to generate a slow phase shift, as seen in Fig. 4(c). Including slow and fast EOPS in a single material may be an attractive attribute of the FN-LC-based platform.

To evaluate the large-scale capability of our EOPS structures, we created a SiP chip with the designed MZM on an area of 0.5 mm^2 . The chip was photonically wire-bonded (PWB) to an external laser source via a fiber array (FA) block. The PWB routes were established using adiabatic surface tapers at the chip edge, followed by selective patterning of FN-LC on active components in a post-processing step. Because of its high viscosity, FN-LC can be applied locally, allowing for more controlled integration with the rest of the chip’s various components, as depicted in Fig. 5. Thanks to the reduced alignment voltage enabled by utilizing FNS waveguides in our Si-FN-LC design, the step can be paired with a V_{DC} , which is used to bias modulators at their quadrature point. Regular EWB and a printed circuit board (PCB) were used to conduct alignment and drive the modulators. A hypothetical EO polymeric version of this chip might necessitate on-chip routing considerations and a separate PCB with high-voltage handling capabilities for poling. It is the only OEO-based SiP chip with >100 modulators that has been reported to our knowledge, which we credit partly to overcoming the poling difficulties by utilizing the poling-free materials described here.

For the first time, we demonstrated GHz-fast EO phase shift and modulation in a novel class of OEO materials, namely ferroelectric nematic liquid crystal. In contrast to EO polymers, we established that the material does not require any electro-thermal poling processes for alignment. Indeed, the material can be oriented during regular modulator RF operation. To simplify the nanofabrication steps, we also engineered the light-matter interaction using a finger-loaded, non-slotted waveguide infiltrated with the material. Using FNS phase shifters as small as $500 \text{ }\mu\text{m}$ in a push-pull MZM, we achieved a DC modulation efficiency of $V_{\pi}L \approx 0.25 \text{ V}\cdot\text{mm}$, an optical ER of $\approx 26 \text{ dB}$, and an insertion loss of $\approx 4 \text{ dB}$. An excellent phase shift efficiency in the order of $\partial n/\partial \kappa \approx 88.9$ was estimated, which we attribute to the material and the FNS waveguide employed in this work. Most importantly, we discovered a high-speed phase shift mechanism with an EO BW $> 4.18 \text{ GHz}$ that outperforms the stronger but slower birefringence effect found in classic paraelectric-nematic liquid crystals. The BW of our FN-LC-covered modulator is limited by the experiment setup, not the suggested devices or the material. Also, an analytical approach was introduced to estimate the Pockels coefficient of the material, where an AC modulation efficiency of $V_{\pi}L \approx 25.7 \text{ V}\cdot\text{mm}$ was obtained owing to a modest $r_{33} \approx 24 \text{ pm/V}$ at $f = 4.18 \text{ MHz}$. As a sufficiently reliable and stable material platform for practical applications that can scale, the comparatively low modulation efficiency at higher speeds for this first-ever prototype is still a breakthrough and a harbinger of further improvements.

The two novelties we combined in this work (the FNS waveguide and the FN-LC material) to create a poling-free Si-organic hybrid platform may lay the foundations for new hybrid photonic integrated circuits with comparable device metrics to those of EO polymers but less stringent post-fabrication steps. One of the main benefits of this result, which has yet to be thoroughly validated, is that no electro-thermal poling step is necessary for the alignment process. Future research will investigate the performance of our proposed poling-free Si-organic modulators based on FN-LC at cryogenic temperatures, which can benefit from better material elasticity.

References

- [1] Shekhar, S., Bogaerts, W., Chrostowski, L., Bowers, J.E., Hochberg, M., Soref, R., Shastri, B.J.: Roadmapping the next generation of silicon photonics. *Nature Communication* **15**(751), 1–15 (2024)
- [2] Xing, Y., Ako, T., George, J.P., Korn, D., Yu, H., Verheyen, P., Pantouvaki, M., Lepage, G., Absil, P., Ruocco, A., *et al.*: Digitally controlled phase shifter using an soi slot waveguide with liquid crystal infiltration. *IEEE Photonics Technology Letters* **27**(12), 1269–1272 (2015)
- [3] Li, J., Chu, D.: Liquid crystal-based enclosed coplanar waveguide phase shifter for 54–66 ghz applications. *Crystals* **9**(12), 650 (2019)
- [4] Capmany, J., Domenech, D., Muñoz, P.: Silicon graphene waveguide tunable broadband microwave photonics phase shifter. *Optics Express* **22**(7), 8094–8100 (2014)
- [5] Sun, H., Qiao, Q., Guan, Q., Zhou, G.: Silicon photonic phase shifters and their applications: A review. *Micromachines* **13**(9), 1509 (2022)
- [6] Jin, C.-Y., Wada, O.: Photonic switching devices based on semiconductor nano-structures. *Journal of Physics D: Applied Physics* **47**(13), 133001 (2014)
- [7] Enami, Y., Luo, J., Jen, A.K.: Short hybrid polymer/sol-gel silica waveguide switches with high in-device electro-optic coefficient based on photostable chromophore. *Aip Advances* **1**(4), 042137 (2011)
- [8] Ali, N., Panepucci, R.R., Xie, Y., Dai, D., Kumar, R.: Electrically controlled 1×2 tunable switch using a phase change material embedded silicon microring. *Applied Optics* **60**(13), 3559–3568 (2021)
- [9] Tahersima, M.H., Ma, Z., Gui, Y., Sun, S., Wang, H., Amin, R., Dalir, H., Chen, R., Miscuglio, M., Sorger, V.J.: Coupling-enhanced dual ito layer electro-absorption modulator in silicon photonics. *Nanophotonics* **8**(9), 1559–1566 (2019)
- [10] Sun, C., Wade, M.T., Lee, Y., Orcutt, J.S., Alloatti, L., Georgas, M.S., Waterman, A.S., Shainline, J.M., Avizienis, R.R., Lin, S., Moss, B.R., Kumar, R., Pavanello, F., Atabaki, A.H., Cook, H.M., Ou, A.J., Leu, J.C., Chen, Y.-H., Asanović, K., Ram, R.J., Popović, M.A., Stojanović, V.M.: Single-chip microprocessor that communicates directly using light. *Nature* **528**(7583), 534–538 (2015)
- [11] Roelkens, G., Liu, L., Liang, D., Jones, R., Fang, A., Koch, B., Bowers, J.: Iii-v/silicon photonics for on-chip and intra-chip optical interconnects. *Laser & Photonics Reviews* **4**(6), 751–779 (2010)

- [12] Sinatkas, G., Christopoulos, T., Tsilipakos, O., Kriezis, E.E.: Electro-optic modulation in integrated photonics. *Journal of Applied Physics* **130**(1), 010901 (2021)
- [13] Gaeta, A.L., Lipson, M., Kippenberg, T.J.: Photonic-chip-based frequency combs. *nature photonics* **13**(3), 158–169 (2019)
- [14] Gui, Y., Nouri, B.M., Miscuglio, M., Amin, R., Wang, H., Khurgin, J.B., Dalir, H., Sorger, V.J.: 100 ghz micrometer-compact broadband monolithic ito mach–zehnder interferometer modulator enabling 3500 times higher packing density. *Nanophotonics* **11**(17), 4001–4009 (2022)
- [15] Amin, R., George, J., Sun, S., Lima, T., Tait, A.N., Khurgin, J., Miscuglio, M., Shastri, B.J., Prucnal, P.R., El-Ghazawi, T., *et al.*: Ito-based electro-absorption modulator for photonic neural activation function. *APL Materials* **7**(8), 081112 (2019)
- [16] Amin, R., Maiti, R., Gui, Y., Suer, C., Miscuglio, M., Heidari, E., Chen, R.T., Dalir, H., Sorger, V.J.: Sub-wavelength ghz-fast broadband ito mach–zehnder modulator on silicon photonics. *Optica* **7**(4), 333–335 (2020)
- [17] Amin, R., Maiti, R., Carfano, C., Ma, Z., Tahersima, M.H., Lilach, Y., Ratnayake, D., Dalir, H., Sorger, V.J.: 0.52 v mm ito-based mach-zehnder modulator in silicon photonics. *Apl Photonics* **3**(12) (2018)
- [18] He, M., Xu, M., Ren, Y., Jian, J., Ruan, Z., Xu, Y., Gao, S., Sun, S., Wen, X., Zhou, L., *et al.*: High-performance hybrid silicon and lithium niobate mach–zehnder modulators for 100 gbit s⁻¹ and beyond. *Nature Photonics* **13**(5), 359–364 (2019)
- [19] Abel, S., Stöferle, T., Marchiori, C., Rossel, C., Rossell, M.D., Erni, R., Caimi, D., Sousa, M., Chelnokov, A., Offrein, B.J., *et al.*: A strong electro-optically active lead-free ferroelectric integrated on silicon. *Nature communications* **4**(1), 1671 (2013)
- [20] Eltes, F., Mai, C., Caimi, D., Kroh, M., Popoff, Y., Winzer, G., Petousi, D., Lischke, S., Ortmann, J.E., Czornomaz, L., *et al.*: A batio 3-based electro-optic pockels modulator monolithically integrated on an advanced silicon photonics platform. *Journal of Lightwave Technology* **37**(5), 1456–1462 (2019)
- [21] Abel, S., Eltes, F., Ortmann, J.E., Messner, A., Castera, P., Wagner, T., Urbonas, D., Rosa, A., Gutierrez, A.M., Tulli, D., *et al.*: Large pockels effect in micro- and nanostructured barium titanate integrated on silicon. *Nature materials* **18**(1), 42–47 (2019)
- [22] Eltes, F., Villarreal-Garcia, G.E., Caimi, D., Siegwart, H., Gentile, A.A., Hart, A., Stark, P., Marshall, G.D., Thompson, M.G., Barreto, J., *et al.*: An integrated optical modulator operating at cryogenic temperatures. *Nature Materials* **19**(11), 1164–1168 (2020)
- [23] Miscuglio, M., Adam, G.C., Kuzum, D., Sorger, V.J.: Roadmap on material-function mapping for photonic-electronic hybrid neural networks. *APL Materials* **7**(10), 100903 (2019)
- [24] Taghavi, I., Moridsadat, M., Tofini, A., Raza, S., Jaeger, N.A., Chrostowski, L., Shastri, B.J., Shekhar, S.: Polymer modulators in silicon photonics: review and projections. *Nanophotonics* (2022)
- [25] Xu, H., Elder, D.L., Johnson, L.E., Heni, W., Coene, Y., De Leo, E., Destraz, M., Meier, N., Vander Ghinst, W., Hammond, S.R., *et al.*: Design and synthesis of chromophores with enhanced electro-optic activities in both bulk and plasmonic–organic hybrid devices. *Materials Horizons* **9**(1), 261–270 (2022)
- [26] Burla, M., Hoessbacher, C., Heni, W., Haffner, C., Fedoryshyn, Y., Werner, D., Watanabe, T., Massler, H., Elder, D.L., Dalton, L.R., *et al.*: 500 ghz plasmonic mach-zehnder modulator enabling sub-thz microwave

- photonics. *APL Photonics* **4**(5), 056106 (2019)
- [27] Alloatti, L., Palmer, R., Diebold, S., Pahl, K.P., Chen, B., Dinu, R., Fournier, M., Fedeli, J.-M., Zwick, T., Freude, W., *et al.*: 100 ghz silicon-organic hybrid modulator. *Light: Science & Applications* **3**(5), 173–173 (2014)
- [28] Lu, G.-W., Hong, J., Qiu, F., Spring, A.M., Kashino, T., Oshima, J., Ozawa, M.-a., Nawata, H., Yokoyama, S.: High-temperature-resistant silicon-polymer hybrid modulator operating at up to 200 gbit s⁻¹ for energy-efficient datacentres and harsh-environment applications. *Nature communications* **11**(1), 1–9 (2020)
- [29] Schwarzenberger, A., Kuzmin, A., Eschenbaum, C., Füllner, C., Mertens, A., Johnson, L., Elder, D., Hammond, S., Dalton, L., Randel, S., *et al.*: Cryogenic operation of a silicon-organic hybrid (soh) modulator at 50 gbit/s and 4 k ambient temperature. In: 2022 European Conference on Optical Communication (ECOC), pp. 1–6 (2022). IEEE
- [30] Habegger, P., Horst, Y., Koepfli, S.M., Kohli, M., De Leo, E., Bisang, D., Destraz, M., Tedaldi, V., Meier, N., Del Medico, N., *et al.*: Plasmonic 100-ghz electro-optic modulators for cryogenic applications. In: European Conference and Exhibition on Optical Communication, pp. 1–1 (2022). Optica Publishing Group
- [31] Hammond, S.R., O’Malleya, K.M., Xub, H., Elder, D.L., Lewis, E.J.: Organic electro-optic materials combining extraordinary nonlinearity with exceptional stability to enable commercial applications. In: SPIE Photonics West (2022). SPIE
- [32] Teng, C., Mortazavi, M., Boudoughian, G.: Origin of the poling-induced optical loss in a nonlinear optical polymeric waveguide. *Applied Physics Letters* **66**(6), 667–669 (1995)
- [33] Taghavi, I., Dehghannasiri, R., Fan, T., Tofini, A., Moradinejad, H., Eftekhari, A.A., Shekhar, S., Chrostowski, L., Jaeger, N.A., Adibi, A.: Enhanced poling and infiltration for highly efficient electro-optic polymer-based mach-zehnder modulators. *Optics Express* **30**(15), 27841–27857 (2022)
- [34] Schulz, K.M., Prorok, S., Jalas, D., Marder, S.R., Luo, J., Jen, A.K.-Y., Zierold, R., Nielsch, K., Eich, M.: Mechanism that governs the electro-optic response of second-order nonlinear polymers on silicon substrates. *Optical Materials Express* **5**(8), 1653–1660 (2015)
- [35] Wang, C.-T., Li, Y.-C., Yu, J.-H., Wang, C.Y., Tseng, C.-W., Jau, H.-C., Chen, Y.-J., Lin, T.-H.: Electrically tunable high q-factor micro-ring resonator based on blue phase liquid crystal cladding. *Optics express* **22**(15), 17776–17781 (2014)
- [36] Zhang, Z., You, Z., Chu, D.: Fundamentals of phase-only liquid crystal on silicon (lcos) devices. *Light: Science & Applications* **3**(10), 213–213 (2014)
- [37] Ptasinski, J., Kim, S.W., Pang, L., Khoo, I.-C., Fainman, Y.: Optical tuning of silicon photonic structures with nematic liquid crystal claddings. *Optics Letters* **38**(12), 2008–2010 (2013)
- [38] Lavrentovich, O.D.: Ferroelectric nematic liquid crystal, a century in waiting. *Proceedings of the National Academy of Sciences* **117**(26), 14629–14631 (2020)
- [39] Chen, X., Korblova, E., Dong, D., Wei, X., Shao, R., Radzihovsky, L., Glaser, M.A., MacLennan, J.E., Bedrov, D., Walba, D.M., *et al.*: First-principles experimental demonstration of ferroelectricity in a thermotropic nematic liquid crystal: Polar domains and striking electro-optics. *Proceedings of the National Academy of Sciences* **117**(25), 14021–14031 (2020)

- [40] Folcia, C.L., Ortega, J., Vidal, R., Sierra, T., Etxebarria, J.: The ferroelectric nematic phase: an optimum liquid crystal candidate for nonlinear optics. *Liquid Crystals* **49**(6), 899–906 (2022)
- [41] Xia, R., Zhao, X., Li, J., Lei, H., Song, Y., Peng, W., Zhang, X., Aya, S., Huang, M.: Achieving enhanced second-harmonic generation in ferroelectric nematics by doping d- π -a chromophores. *Journal of Materials Chemistry C* **11**(32), 10905–10910 (2023)
- [42] Ding, R., Baehr-Jones, T., Liu, Y., Bojko, R., Witzens, J., Huang, S., Luo, J., Benight, S., Sullivan, P., Fedeli, J., *et al.*: Demonstration of a low v π l modulator with ghz bandwidth based on electro-optic polymer-clad silicon slot waveguides. *Optics Express* **18**(15), 15618–15623 (2010)
- [43] Melikyan, A., Alloatti, L., Muslija, A., Hillerkuss, D., Schindler, P.C., Li, J., Palmer, R., Korn, D., Muehlbrandt, S., Van Thourhout, D., *et al.*: High-speed plasmonic phase modulators. *Nature Photonics* **8**(3), 229–233 (2014)
- [44] Pan, Z., Xu, X., Chung, C.-J., Dalir, H., Yan, H., Chen, K., Wang, Y., Jia, B., Chen, R.T.: High-speed modulator based on electro-optic polymer infiltrated subwavelength grating waveguide ring resonator. *Laser & Photonics Reviews* **12**(6), 1700300 (2018)
- [45] Inoue, S.-i., Otomo, A.: Electro-optic polymer/silicon hybrid slow light modulator based on one-dimensional photonic crystal waveguides. *Applied Physics Letters* **103**(17), 171101 (2013)
- [46] Ummethala, S., Kemal, J.N., Alam, A.S., Lauermann, M., Kuzmin, A., Kutuvantavida, Y., Nandam, S.H., Hahn, L., Elder, D.L., Dalton, L.R., *et al.*: Hybrid electro-optic modulator combining silicon photonic slot waveguides with high-k radio-frequency slotlines. *Optica* **8**(4), 511–519 (2021)
- [47] Witmer, J.D., McKenna, T.P., Arrangoiz-Arriola, P., Van Laer, R., Wollack, E.A., Lin, F., Jen, A.K., Luo, J., Safavi-Naeini, A.H.: A silicon-organic hybrid platform for quantum microwave-to-optical transduction. *Quantum Science and Technology* **5**(3), 034004 (2020)
- [48] Wang, G., Baehr-Jones, T., Hochberg, M., Scherer, A.: Design and fabrication of segmented, slotted waveguides for electro-optic modulation. *Applied Physics Letters* **91**(14), 143109 (2007)
- [49] Hochberg, M., Baehr-Jones, T., Walker, C., Witzens, J., Gunn, L.C., Scherer, A.: Segmented waveguides in thin silicon-on-insulator. *JOSA B* **22**(7), 1493–1497 (2005)
- [50] Gould, M., Baehr-Jones, T., Ding, R., Huang, S., Luo, J., Jen, A.K.-Y., Fedeli, J.-M., Fournier, M., Hochberg, M.: Silicon-polymer hybrid slot waveguide ring-resonator modulator. *Optics express* **19**(5), 3952–3961 (2011)
- [51] Xu, H., Liu, F., Elder, D.L., Johnson, L.E., Coene, Y., Clays, K., Robinson, B.H., Dalton, L.R.: Ultrahigh electro-optic coefficients, high index of refraction, and long-term stability from diels-alder cross-linkable binary molecular glasses. *Chemistry of Materials* **32**(4), 1408–1421 (2020)
- [52] Witt, D., Young, J., Chrostowski, L.: Reinforcement learning for photonic component design. *APL Photonics* **8**(10) (2023)
- [53] Darcie, A., Mitchell, M., Awan, K., Abdolahi, M., Hammood, M., Pfenning, A., Yan, X., Affi, A., Witt, D., Lin, B., *et al.*: Siepicfab: the canadian silicon photonics rapid-prototyping foundry for integrated optics and quantum computing. In: *Silicon Photonics XVI*, vol. 11691, pp. 31–50 (2021). SPIE
- [54] Wang, Y., Yun, H., Lu, Z., Bojko, R., Shi, W., Wang, X., Flueckiger, J., Zhang, F., Caverley, M., Jaeger, N.A., *et al.*: Apodized focusing fully etched subwavelength grating couplers. *IEEE Photonics Journal* **7**(3),

1–10 (2015)

- [55] Yamaguchi, Y., Dat, P.T., Takano, S., Motoya, M., Hirata, S., Kataoka, Y., Ichikawa, J., Oikawa, S., Shimizu, R., Yamamoto, N., et al.: Traveling-wave mach–zehnder modulator integrated with electro-optic frequency-domain equalizer for broadband modulation. *Journal of Lightwave Technology* (2023)
- [56] Taghavi, I., Dehghanasiri, R., Fan, T., Moradinejad, H., Taghinejad, H., Hosseinnia, A.H., Eftekhari, A.A., Adibi, A.: Enhanced polling and infiltration of highly-linear mach-zehnder modulators on si/sin-organic hybrid platform. In: *CLEO: Science and Innovations*, pp. 1–1 (2018). Optical Society of America
- [57] Park, J.W., You, J.-B., Kim, I.G., Kim, G.: High-modulation efficiency silicon mach-zehnder optical modulator based on carrier depletion in a pn diode. *Optics express* **17**(18), 15520–15524 (2009)
- [58] Qiu, F., Sato, H., Spring, A.M., Maeda, D., Ozawa, M.-a., Odoi, K., Aoki, I., Otomo, A., Yokoyama, S.: Ultra-thin silicon/electro-optic polymer hybrid waveguide modulators. *Applied Physics Letters* **107**(12), 92–1 (2015)

Acknowledgements

The Natural Sciences and Engineering Research Council of Canada (NSERC), the SiEPICfab consortium, the B.C. Knowledge Development Fund (BCKDF), the Canada Foundation for Innovation (CFI), MITACS, and the Schmidt Sciences funded this research.

Data availability

The supporting data for the conclusions of this investigation are available upon reasonable request.

Author contribution

This work was conceptualized by I.T., L.C., S.S. C.P., J.S., and N.J. contributed materials and technical information, while S.J., D.W. and I.T. built the organic Si modulator described in this paper. I.T. conducted measurements while N.J. and O.E. helped with the modulator measurement setup. The manuscript was written by I.T., L.C., and S.S., with assistance from all authors.

Methods

Device fabrication: The modulators were patterned on a standard 220 nm silicon on an insulator wafer with a buried oxide layer of 3.5 μm . An electron beam lithography tool (JBX-8100FS) was used to design the waveguides via positive tone resist (ZEP 520A-7) [53, 54].

After that, the devices were dry-etched with an ICP plasma etcher tool (Oxford COBRA). Using maskless lithography (Heidelberg MLA-150), metal electrodes (100 nm gold atop 5 nm titanium as an adhesion layer) were deposited 4.85 μm distant from the core waveguide. A passive optical measurement was performed for reference after completing the nanofabrication stages of photonic-only structures and before metallization.

After metallization, both chips were cleaned gently using acetone, IPA, DI water, and a N_2 gun, followed by a ≈ 30 sec oxygen plasma cleaning for surface passivation just before coating. For the OEO cladding, we used PM-158 (a proprietary FN-LC material optimized for enhanced $\chi^{(2)}$ obtained from Polaris Electro-Optics, Inc.). According to our pre-coating viscosity experiments, the cleaned chips benefitted from being warmed up (70-80°C) to reduce the viscosity of FN-LC during application to the chip. A glass capillary tube was used to apply enough FN-LC to the desired areas. Finally, the chips were cooled to 25°C before characterization.

FN-LC alignment and DC characterization: While no significant relationship was found between the timing of the alignment stage and the time passed after coating FN-LC, the alignment step was performed on the same day. After coating, the produced samples were mounted on an active EO probe station with temperature control. A source meter unit (Keithley 2400) was employed to apply step voltage. The light from a tunable CW laser (Agilent 8164A/81682A) is coupled into grating couplers using an 8-degree polished angle FA. In this phase, we tune the laser wavelength to the highest peak achievable by overlapping the MZM spectrum with that of the GC or PWB. An InGaAs power sensor (Agilent 81635A) detects light. Finally, the components of phase shift efficiency (i.e., $\partial n/\partial v$ and $\partial \kappa/\partial v$) were extracted using the associated shifts in the vertical (P_{out}) and horizontal (λ) directions as a function of applied voltage.

AC characterization: An 18 GHz vector network analyzer (Keysigth FieldFox VNA) was added for AC characterization, with port 1 amplified using a microwave amplifier (SHF-s807). It is mixed with a proper amount of DC voltage for optimum MZM performance and simultaneously for FN-LC alignment. A high-speed photodetector (Thorlabs RXM40AF) was employed at the output, along with low-noise amplifiers (picosecond 5828). The VNA data was utilized to evaluate the device S -parameters. The devices were aged at a regulated temperature (25°C) for ≈ 150 hours with no humidity control or hermetic sealing applied, with light ($P_{\text{opt,in}} = 8$ dBm) and an RF electrical signal ($v = 1.59$ V) applied.

The material EO coefficient of FN-LC (i.e., r_{33}) was post-processed using the analytical formula [50]:

$$S_{21} = 20 \times \log \left[\alpha_{\text{opt}} \times \frac{\partial(p_{\text{mod}})}{\partial(n)} \frac{\partial(n)}{\partial(v)} \frac{\partial(v_{\text{det}})}{\partial(p_{\text{det}})} \times G_{\text{RF}} \right] \quad (1)$$

where G_{RF} is the calibrated gain of the modulator link, α_{opt} is the total optical loss, p_{mod} is the optical output of the MZM, p_{det} (v_{det}) is the optical (electrical) input (output) of the detector, n is the effective index of the FNS waveguide covered with FN-LC, and v is the MZM drive voltage, respectively. Here, $\partial(v_{\text{det}})/\partial(p_{\text{det}})$ and $\partial(n)/\partial(v)$ correspond to the detector and the MZM sensitivities. The latter is related to V_{π} and, finally, to r_{33} by:

$$V_{\pi} = \frac{\lambda}{2L} \left[\frac{\partial(n)}{\partial(v)} \right]^{-1}, \quad (2)$$

$$r_{33} = \frac{2d}{n^3\Gamma} \left[\frac{\partial(n)}{\partial(v)} \right] \quad (3)$$

where d denotes the distance between the tip of two encountering fingers and Γ is the overlap integral between optical (\hat{E}_x) and electrical (\vec{E}_e) modal fields [56] evaluated by:

$$\Gamma = \frac{1}{Z_0} \iiint_V n_{\text{eff}}(\vec{E}_e) |\hat{E}_x|^2 / \iint_A L \times \text{Re}(\hat{E} \times \hat{H}^*) \quad (4)$$

In Equation 4, n_{eff} is the field-dependent effective mode index of FNS waveguide, A and V are the cross-section and volume of the gap between fingers tip and core waveguide, Z_0 is the free space impedance, and \hat{H} is the magnetic field of the optical mode, respectively.

	EO polymer	Organic NLO ¹	PN-LC ²	FN-LC ³
Non-zero second-order susceptibility, $\chi^{(2)}$	●	●		●
Non-centro symmetric crystal lattice	●	●		●
Spontaneous molecular organization		●	●	●
Alignments using interface layer or small \hat{E}_x			●	●
Reorientation of slow/fast axes in response to external \hat{E}_x			●	●
Large spontaneous polarizations and second order nonlinearities				●

Table 1: OEO material comparison

¹ Nonlinear optic

² Paraelectric nematic liquid crystal

³ Ferroelectric nematic liquid crystal

Topology	Phase shift material	Size ² (mm)	V_π (V)	$V_\pi L\alpha$ (V.dB)	ER_{opt} (dB)	$\partial n/\partial v$ (V^{-1})	$\partial \kappa/\partial v$ (V^{-1})	Ref.
MZM	LNOI	3	7.4	2.18	40	6.98×10^{-5}	-	[18]
MZM ¹	ITO	0.03	16	80	-	1.47×10^{-3}	1.64×10^{-3}	[17]
MZM	BTO	2	1.15	1.3	-	3.37×10^{-4}	1.37×10^{-5}	[20]
MZM	doped Si	2	9	79.2	12.5	3.89×10^{-4}	2.54×10^{-5}	[57]
Slot-MZM	EO polymer	13	4.6	23.92	-	2.59×10^{-5}	-	[58]
Slot-MZM	EO polymer	8	1.8	3.17	-	1.07×10^{-4}	-	[28]
FNS-MZM	FN-LC	0.5	0.5* (51.4**)	2* (413.6**)	26	4.04×10^{-3}	4.54×10^{-5}	this work

Table 2: EO Modulator comparison

¹ Electro-absorption modulator

² Arm length of an MZM

* DC metrics

** AC metrics

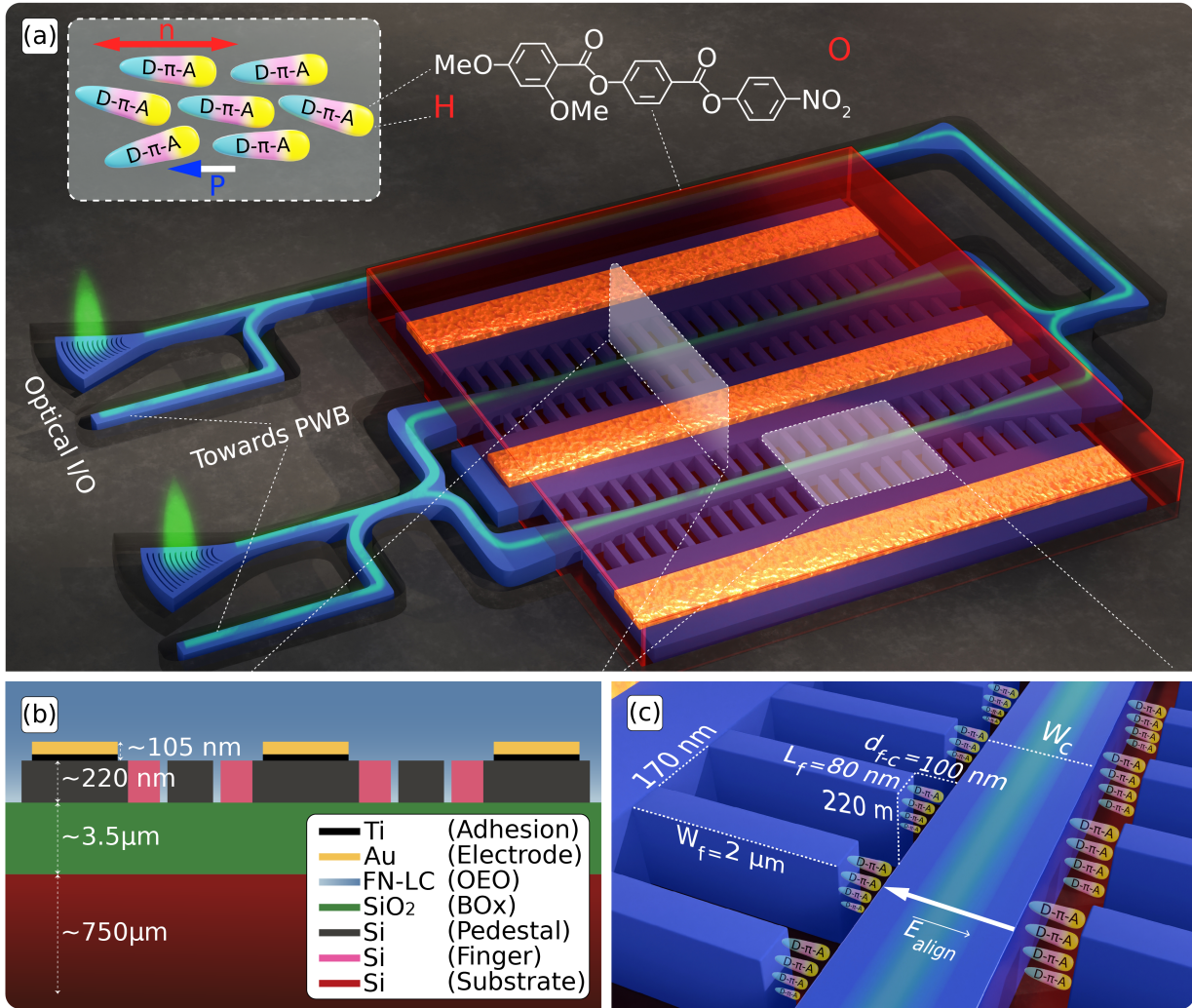


Figure 1: 3D representation of the modulator selectively covered by FN-LC. **a** 80-nm-wide fingers are used to carry the RF signals and alignment field (E_{align}) to an area as close as $d_{f-c} = 100$ nm away from the $W_c = 300$ nm-wide core. This design optimizes the overlap integral between the optical and electrical fields (Γ) while minimizing optical loss. An external light source, either through a grating coupler or a photonic wirebond (PWB), feeds the optical signal. The waveguides are identified by a 2 μm trench that surrounds them. A positive-tone ebeam resist patterns the device. **Inset:** An illustrative chemical structure and polar order of dipolar constituents of the FN-LC phase, where n denotes the molecular director, P is the polarization, and $D - \pi - A$ is the donor-bridge-acceptor electronic structure. **b** The layer stack-up of the MZM consists of two FNS waveguides in each arm. **c** A zoomed-in diagram of the FNS waveguide with infiltrated FN-LC ordered along E_{align} .

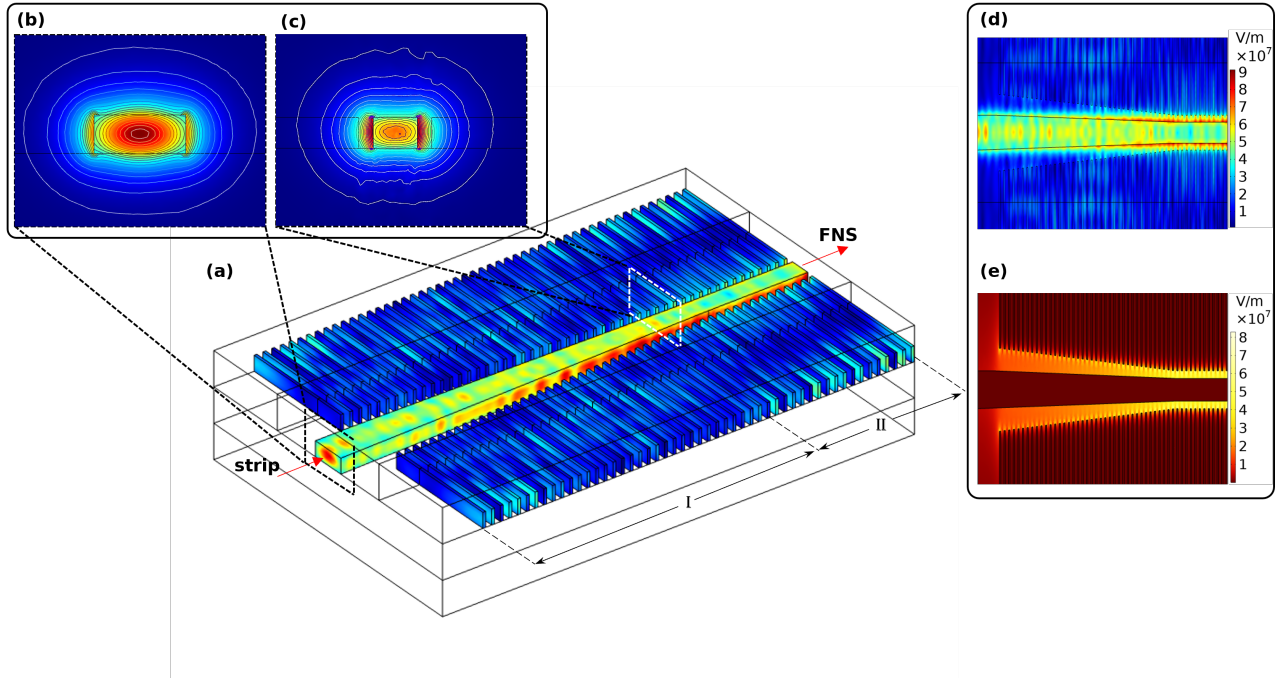


Figure 2: Waveguide design simulation results. **a** The mode evolution in each arm of the MZM demonstrated by a $10 \mu\text{m}$ -long adiabatic strip-to-finger mode converter (section I) coupled to a $3 \mu\text{m}$ -long portion of the $500 \mu\text{m}$ FNS waveguide (section II). Transverse electric optical field (\hat{E}_x) in x -slice ($x = 0$ nm) sampled **b** before and **c** after the converter, which represents non-slotted and FNS geometries, respectively. \hat{E}_x is further decentralized when the core section is shrunk to $W_c = 300$ nm because it is pushed to the two gaps surrounding it, where normalized electrical field (\vec{E}_e) and FN-LC coexist. **d** \hat{E}_x and **e** \vec{E}_e in the y -slice perspective ($y = 110$ nm). Compared to a non-slotted waveguide, the LMI-engineered FNS waveguide acts like a double-slot waveguide to offer ≈ 10 times improvement in \vec{E}_e as a result of improved electrode distance as well as ≈ 2 times higher Γ .

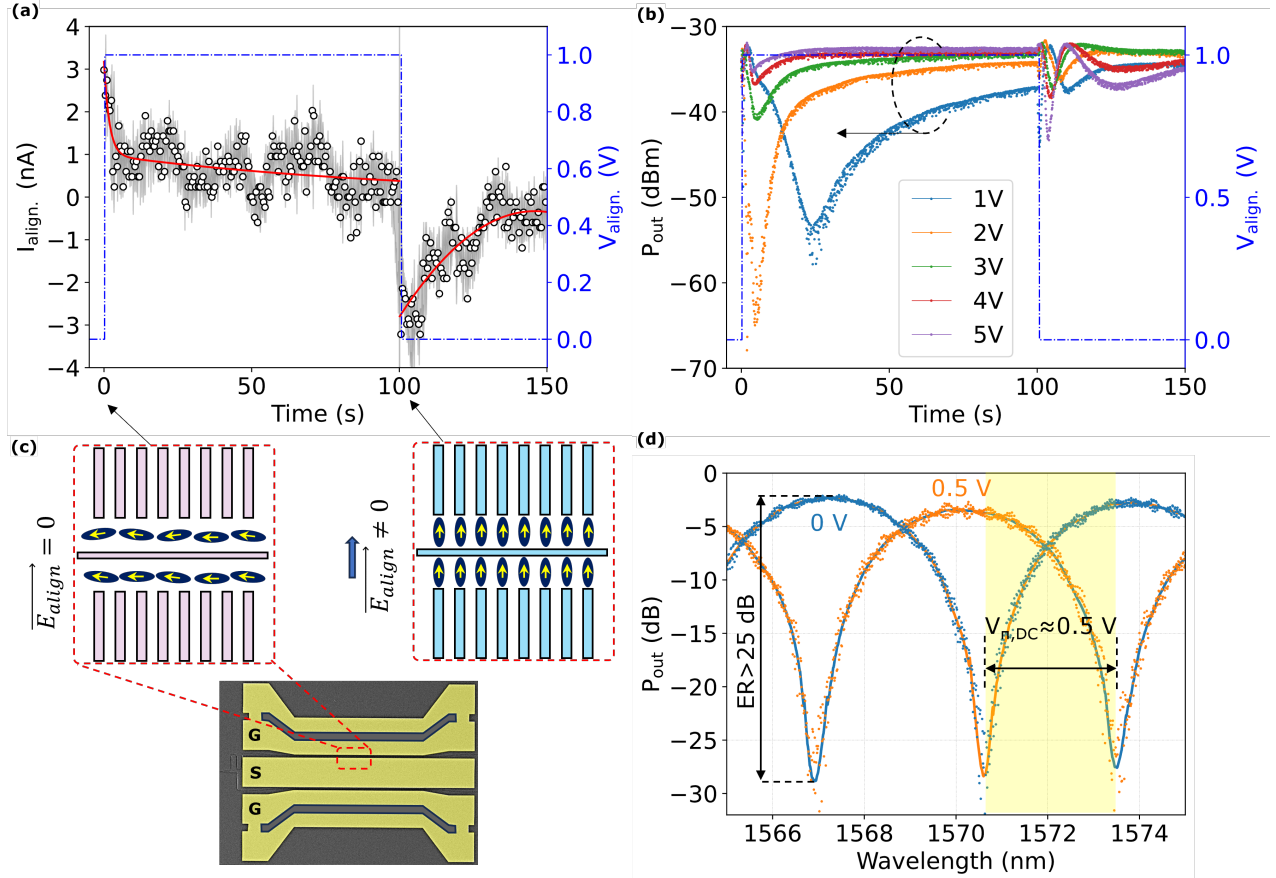


Figure 3: FN-LC alignment. **a** Polarization-originated leakage current and **b** optical output in response to an external electric field ($\vec{E}_{\text{align}} \propto V_{\text{align}}/[d_{f-c} + W_c]$) applied to the MZM arms. The measurement is repeated with increasing V_{align} until complete domain formation is achieved. **c** A microscopic image of the MZM along with the dipolar order of FN-LC in a section of its FNS waveguide in the cases of $\vec{E}_{\text{align}} \neq 0$ and $\vec{E}_{\text{align}} = 0$ (other possibilities for dipolar order could exist, since we don't know what the ground state is with this topology). **d** Optical output spectrum (normalized) versus applied voltage exhibiting changes in the EOPS complex refractive index ($n + ik$ where $\Delta n \gg \Delta \kappa$ for an ideal EOPS). The data is summarized in Table 2.

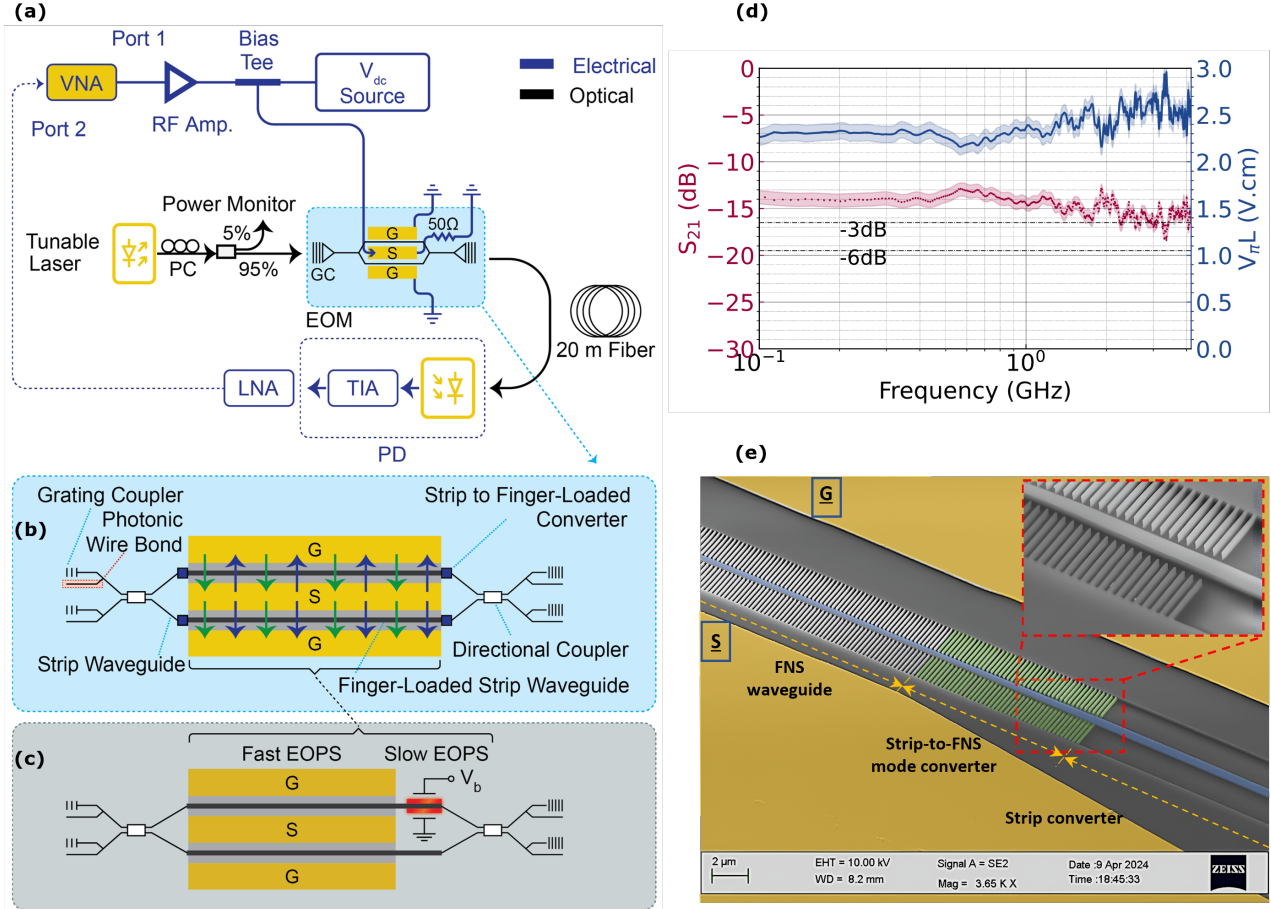


Figure 4: Device characterizations. **a** Experimental setup using a VNA and appropriate amplification to drive FN-LC MZM in push-pull configuration. The DC voltage (V_{DC}) applied to bias the modulator at its quadrature point can also be used to replace the alignment step (i.e., Fig. 3a-b). **b** MZM schematic showing two 500 μm -long EOPS and low-loss strip-to-finger-loaded mode converters equipped with GC and PWB optical I/O channels. The alignment has been performed unipolarly, as evidenced by the green arrows. However, the RF field is applied bipolarly to achieve push-pull performance, as the dark blue arrows show. The proposed EOPS made of FN-LC incorporates both slow and fast phase shift mechanisms compared to the conventional approach, shown in **c**, in which an inefficient thermo-optic effect is required in conjunction with a fast EOPS for advanced modulation schemes. **d** Measured S_{21} reveals the existence of a high-speed phase shift mechanism with an EO BW of $f_{-6\text{dB}} > 4.18$ GHz. Post-processed AC values of $V_{\pi}L$ based on extracted r_{33} as a function of frequency are also shown. **e** A false-colored scanning electron microscope (SEM) image of the LMI-engineered FNS waveguide with a zoomed-in view of its mode converter.

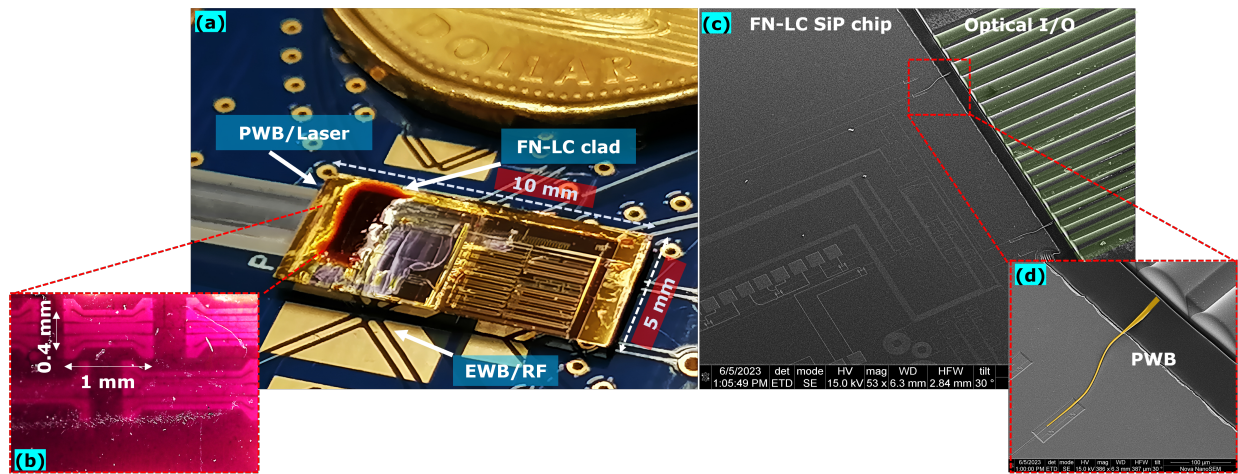


Figure 5: FN-LC-enabled silicon photonic chip. **a** A close-up picture of the chiplet incorporating 108 FN-LC MZMs, the majority of which occupies a footprint of 0.4 mm^2 . EWBs are used to carry RF signals at the chip level. FN-LC has been selectively applied to a cluster of MZMs on the left for demonstration purposes. Top-down GC and the PWB handle optical I/O for tests at device and chip level, respectively. **b** A microscopic zoomed-in view of the FN-LC-enabled modulators of various EOPS lengths. **c** An SEM picture shows PWBs as extra optical I/O paths and their adiabatic surface tapers for low-loss power coupling. A 3D laser printer tool (Vanguard Automation - Sonata 1000) uses the two-photon polymerization effect to create free-form optical waveguides. The FN-LC needs to cover the EOPS sections on the SiP chip, leaving adequate space for the polymer required for PWB construction. **d** A magnified, false-colored SEM view of the PWB waveguide created between fibers and the on-chip surface taper.